# AN EXPERIMENTAL STUDY OF ROTOR/FUSELAGE INTERACTION

Yasutada Tanabe, Shigeru Saito, Noboru Kobiki and Katsuichi Murota
Japan Aerospace Exploration Agency, Chofu, Tokyo, JAPAN

Hideaki Sugawara
Ryoyu Systems Co., LTD., Nagoya, JAPAN
and
Kyohei Hayashi, Katsumi Hiraoka
Graduate School, Tokai University, Hiratsuka, Kanagawa, JAPAN

**Abstract**

Rotor/Fuselage Interaction remains as an important problem for engineers and scientists working on helicopter aerodynamics. A model rotor test stand (JAXA Multi-purpose Rotor Test Stand, JMRTS) is used to build an experimental database for CFD code validations. Four blades are connected to an articulated rotor hub. Feathering, flapping and lead-lag angles at the hinges are measured using Hall-sensors which give high accuracy. Miniature Kulite pressure sensors are installed on the cowling surface which simulate a type of helicopter fuselages. Time-averaged and ensemble-averaged periodic data are obtained. Good correlations were obtained in the measured results between the blade angles and six-component forces and moments as well as the pressure fluctuations on the fuselage and blade surfaces. Datasets of several selected test cases are presented together with geometric descriptions of the blade and the fuselage to enable CFD validations by other parties.

## 1. INTRODUCTION

Rotor/Fuselage Interaction remains as an important problem for engineers and scientists working on helicopter aerodynamics. Because of the rotor downwash, periodic airloads impact on the fuselage which cause vibration and noise inside the passenger cabin. Also the fatigue life of the airframe is influenced. Detailed experimental data of ROBIN (ROtor Body INteraction) configuration[1)] have been published and they become representative test cases for CFD method validations. Besides this configuration, few data with other realistic helicopter fuselage configurations are available. A very simple model was used in Georgia-Tech (called GT-model) to study the interference between a rotor and a cylinder body[2)]. A Dauphin 365N helicopter model was used in ONERA to investigate the rotor-fuselage aerodynamic interaction problem[3)].

JAXA is working on an integrated CFD-based comprehensive analysis tool for low noise rotor design. A model rotor stand (JAXA Multipurpose Rotor Test Stand, JMRTS) is used to build an experimental database for the CFD code validations. This rotor stand has been used for BVI studies and other tests[4-6)] till now. Four blades are installed through an articulated rotor hub. Feathering, flapping and lead-lag angles at the hinges are measured with Hall-sensors which give high S/N ratios compared with potentiometers used before. Miniature Kulite pressure sensors are intalled on the cowling surface which simulate a type of helicopter fuselages.

Experiments were carried out in November 2008. Simple time-averaged and ensemble averaged periodic data are obtained. Good correlations were obtained in the measured results between the blade angles and six-components forces and moments as well as the pressure fluctuations on the fuselage and blade surfaces. Flight conditions include hovering, and forward flight up to advance ratio of 0.3. The whole model was tilted from forward -2 deg to backward 4 deg to simulate the general forward flight and descending flight where BVI occurs. Datasets of selected forward flight condition cases are presented together with the geometric descriptions of the rotor blade and the fuselage to enable CFD validations by other parties.

## 2. EXPERIMENTAL APPARATUS

### 2.1. Wind tunnel

Experiments were carried out in JAXA 6.5m x 5.5m Low-speed Wind Tunnel in November, 2008. This wind tunnel is a closed circuit, continuous atmospheric tunnel with free stream velocity of 1 ~ 70 m/s. The test section is a closed-wall-type with 6.5 m in height and 5.5 m in width. The rotor system is mounted with a strut to place the rotor centre in the centre of the test section. Hovering tests were carried out inside the closed wall test section. Although the rotor diameter of about 2m is relative small compared with the test section size, air circulations were expected that may have influences on the hovering test results. For experiments with relatively high advance ratios, the influences of the test section walls are considered small. Future CFD study of the effects of the test section walls is expected.

### 2.2. JAXA Multi-purpose Rotor Test Stand (JMRTS)

Figure 1 shows the JAXA Multi-purpose Rotor Test Stand (JMRTS) installed inside the test section. This rotor test stand was designed to drive different-types of rotors in the wind tunnel for measuring aerodynamic and acoustic characteristics of the rotors. In the present test, a rotor with four 1.021 m radius, rectangular blades are connected to the rotor head by hinges to allow flapping, lead-lagging and feathering motions. All the three hinges have a common hinge centre with offset of 44.5 mm. The wing section of the blade is NACA0012 with a chord length of 6.5 cm. Two blades have unsteady pressure sensors and other two blades have strain gauges installed. The linear twist angle for the blades is -8 deg/m. All the pitch angles are referred to that at the blade root where r=21 mm. Root-cut is at 206 mm (20.2%R). The flapping inertia moment of the blade is $I_b = 0.186 kg \cdot m^2$ with the blade grip. Total mass is 2.4 kg together with the grip while 0.74 kg is for the blade itself. Illustration of the blade is shown in Figure 2.

The side view of the rotor stand is shown in Figure 3. The height of the rotor centre is at the centre of the wind tunnel test section. The layout of the main components of the rotor stand is shown in Figure 4. The rotor shaft angle can only be changed together with the fuselage attitude. Rotor is driven with a water-cooled electric motor with a maximum output of 37 hp.

### 2.3. Fuselage model

The cowling for the rotor stand was designed to be similar to one type of the representative helicopter fuselage designs. The fuselage nose extrudes ahead and the fuselage surface curvature has an abrupt change at the junction line formed by the nose and the body. Compared with ROBIN shape, current shape is more realistic and more complicated. Totally 15 positions at the upper and side surfaces are selected where the miniature Kulite high response pressure sensors are placed in a line on the upper surface center longitudinally and a line at the fore body laterally.

The shape of the fuselage is shown in Figure 5 where the contour lines are given. Rotor center is at the axis origin. The pressure sensor positions are shown in Figure 6 and tabulated in Table 1.

### 2.4. Sensors and measurements

New blade angle sensors are installed to improve the accuracy in the measurement of the blade motions. Hall-sensors are placed at the hinges to directly measure the flapping / lead-lagging and feathering angles. Good linearity is obtained in the calibrations. However, output offset of the flapping angle sensor is found to be influenced by the centrifugal forces. Calibration test with several different rotating speeds is carried out and a empirical compensation curve is obtained.

The unsteady pressure sensors installed in the rotor blade are gauge-types. Increasing offset is observed with higher rotating speed. Pressure variations around the average are obtained. Typical oscillations are observed at the BVI test conditions.

The elastic deformations of the blades are not measured during the test. Because a full articulated hub is used, the elastic deformations of the blades are considered small. The effects will be studied numerically and/or experimentally in the future.

Totally 32 channels of data are recorded during the test as shown in Table 2. Wind tunnel testing conditions necessary for data reductions are recorded separately at the same time.

## 3. EXPERIMENTAL METHODS

### 3.1. Test conditions

Test conditions for all of the related RUNs are summarized in Table 3. In this report, we will concentrate mainly on the forward flight case with tip Mach number of 0.56 (RUN009).

### 3.2. Data processing

The outputs of the sensors are recorded with 16-bits A/D converters. The initial offsets are removed from the data then all the data are converted into physical values with calibrated factors. The outputs from the 6-component balance are converted into forces and moments in each axis with corrections of the interferences from other components using a 6x6 calibration matrix.

For each physical quantity, simple time-averaged values are obtained at first. To obtain the periodically time-varying values per each revolution, ensemble averaging is performed based on the pulse signal once a revolution. Every data record consists of 5 seconds of data sampled at 50kHz. The rotating speed may have small variations during the recording time. As a result, the data number between the pulses may differ by about $\pm 3$ for a typical 1667 samplings when the rotor is running at 1800 rpm where 150 periods are included. Ensemble-averaging are performed by defining a common azimuth angle step (0.5 deg in this report) and averaging the interpolated values from each rotation. Typical effect of this processing is shown in Figure 7 and we can see the obtained ensemble-averaged variations are smoother than the original instantaneous 1-period data and the signal uncertainties caused by random noise are removed.

## 4. RESULTS AND DISCUSSIONS

### 4.1. CT-CQ curve at hover

Hovering CT-CQ curve for different tip Mach number are shown in Figure 8. Although some small differences are found at the low CT range, good agreement are found between these two different tip Mach numbers elsewhere.

### 4.2. Averaged surface pressure

RUN011 is selected as a representative case of forward flight. Detailed test conditions and rotor control and blade motion data are shown in Table 4. In this table, $C_{pa}$ is referred to sonic speed and defined as:

(1) $$C_{pa} = \frac{p - p_\infty}{\frac{1}{2}\rho_\infty a_\infty^2}$$

Only 1st harmonic coefficients of the blade angles are tabulated. The pitch angle is:

(2) $$\theta(\Psi) = \theta 0 + \theta 1 * \cos\Psi + \theta 2 * \sin\Psi$$

so that $A1 = -\theta 1$, and $B1 = -\theta 2$. The flapping angle is:

(3) $$\beta(\Psi) = \beta 0 + \beta 1 * \cos\Psi + \beta 2 * \sin\Psi$$

and the lead-lag angle is defined as positive forward:

(4) $$\varsigma(\Psi) = \varsigma 0 + \varsigma 1 * \cos\Psi + \varsigma 2 * \sin\Psi$$

A periodically ensemble-averaged sample of the blade angles is given in Figure 9. Also the reconstructed signals with only the first harmonics are compared. It can be seen low noise level is attained for these data.

Averaged surface pressure distributions with different advance ratios are shown in Figure 10 where the coefficients of pressure are referred to freestream velocities as:

(5) $$C_{p\infty} = C_{pa} / M_\infty^{\ 2}$$

Please note that in Table 4, the first row is for hovering case with a different $C_T$ setting. This have been done to avoid over-current for the drive motor. This row of data must be excluded when making trend study under a constant $C_T$ condition.

### 4.3. Periodic surface pressure variation

The ensemble-averaged periodic surface pressure variations for different advance ratios are shown in Figure 11. It can be seen as the advance ratio increases, pressure fluctuations also increase. Especially, at position Pbody04 and Pbody08, the pressure oscillations are remarkably high for advance ratio of 0.29.

In the longitudinal line, azimuth angles where the peaks observed are almost the same. But for the pressures in the lateral line, significant phase differences are observed with regard to the blade-passing in the order of 10 -> 09 -> 08 -> 04 -> 07 -> 06 -> 05.

Behind the rotor hub, pressure sensor position 11-15, turbulent fluctuations were observed in the instantaneous pressure signals. Flow separation and influence of the rotor shaft are expected.

## 5. CONCLUSION

An experimental study of Rotor/Fuselage Interaction using JMRTS (JAXA Multi-purpose Rotor Test Stand) is conducted. Blade angles are obtained with good accuracy. Besides the averaged six component balance data, periodically ensemble-averaged pressure variations on the fuselage surface are also obtained. Descriptions about the rotor blade and fuselage shape are provided to enable CFD validations.

## REFERENCES

[1] Mineck, R. E., et al, "Steady and Periodic Pressure Measurement on a Generic Helicopter Fuselage Model in the Presence of a Rotor," NASA TM-2000-210286, June 2000.

[2] Liou, S.G., et al, "Measurement of the Interaction Between a Rotor Tip Vortex and a Cylinder," AIAA Journal, Vol.28, No.6, June 1990.

[3] A. Le Pape, J. Gatard and J.-C. Monnier, "Experimental Investigations of Rotor-Fuselage Aerodynamic Interactions", J. AHS, April 2007.

[4] Kenta Masaki, et al, "Wind Tunnel Test for BVI Noise and Vibration Reduction Using Blade Active Control," 31st ERF, Sept. 13-15, 2005, Florence, Italy.

[5] Hiroyuki Kato, et al., "Application of Stereoscopic PIV to Helicopter Rotor Blade Tip Vortices," 20th International Congress on Instrumentation in Aerospace Simulation Facilities, Aug. 25-29, 2003, DLR Gottingen, Germany.

[6] Kenichiro Nagai, et al., "Array Measurement Techniques for Noise Source Location of Helicopter Main Rotor Noise, " InterNoise2003,

Table 1 : Coordinates of locations of unsteady surface pressure sensors

| No | X [m] | Y [m] | Z [m] |
|---|---|---|---|
| Pbody01 | −0.680 | 0 | −0.459 |
| Pbody02 | −0.526 | 0 | −0.285 |
| Pbody03 | −0.369 | 0 | −0.213 |
| Pbody04 | −0.212 | 0 | −0.068 |
| Pbody05 | −0.212 | −0.207 | −0.125 |
| Pbody06 | −0.212 | −0.167 | −0.083 |
| Pbody07 | −0.212 | −0.112 | −0.066 |
| Pbody08 | −0.212 | 0.111 | −0.067 |
| Pbody09 | −0.213 | 0.165 | −0.081 |
| Pbody10 | −0.213 | 0.205 | −0.120 |
| Pbody11 | 0.257 | 0 | −0.072 |
| Pbody12 | 0.412 | 0 | −0.141 |
| Pbody13 | 0.569 | 0 | −0.214 |
| Pbody14 | 0.725 | 0 | −0.258 |
| Pbody15 | 0.880 | 0 | −0.402 |

Table 2: Data sampling channels

| Ch | Nomenclature | Range |
|---|---|---|
| 01 | Fx | ± 5V |
| 02 | Fy | ± 5V |
| 03 | Fz | ± 5V |
| 04 | Mx | ± 5V |
| 05 | My | ± 5V |
| 06 | Mz | ± 5V |
| 07 | Pbody01 | ± 10V |
| 08 | Pbody02 | ± 10V |
| 09 | Pbody03 | ± 10V |
| 10 | Pbody04 | ± 10V |
| 11 | Pbody05 | ± 10V |
| 12 | Pbody06 | ± 10V |
| 13 | Pbody07 | ± 10V |
| 14 | Pbody08 | ± 10V |
| 15 | Pbody09 | ± 10V |
| 16 | Pbody10 | ± 10V |

| Ch | Nomenclature | Range |
|---|---|---|
| 17 | Pbody11 | ± 10V |
| 18 | Pbody12 | ± 10V |
| 19 | Pbody13 | ± 10V |
| 20 | Pbody14 | ± 10V |
| 21 | Pbody15 | ± 10V |
| 22 | Pblade11 | ± 10V |
| 23 | Pblade12 | ± 10V |
| 24 | Pblade13 | ± 10V |
| 25 | Pblade14 | ± 10V |
| 26 | SGblade1 | ± 10V |
| 27 | Gsensor1 | ± 5V |
| 28 | Rotation | ± 5V |
| 29 | B1_Flap | ± 5V |
| 30 | B2_Pitch | ± 5V |
| 31 | B1_LdRg | ± 5V |
| 32 | Pulse | ± 5V |

Table 3: Test conditions

| RUN NO. | Test Title | Case Numbers | Date | Wind Tunnel Parameters | | | | | Rotor Parameters | | | | | | | |
|---|---|---|---|---|---|---|---|---|---|---|---|---|---|---|---|---|
| | | | | $V_\infty$ | T | $\rho$ | a | $M\infty$ | $\mu$ | Mtip | $\alpha$ | $C_T$ | $\theta_0$ | $A_1$ | $B_1$ | N |
| | | | | m/s | ℃ | $kg/m^3$ | m/s | | – | | deg | $\times 10^{-3}$ | deg | deg | deg | rpm |
| RUN 001 | Hub drag, Fuselage pressure Measurement | 7 | 08.11/05 | 30・60 | 16.5 | 1.23 | 341 | 0.09・0.18 | 0.29 | 0.3˜0.56 | 0 | | | | | 1000・1950 |
| RUN 002 | Hub drag, Fuselage pressure Measurement | 7 | 08.11/05 | 30・60 | 17.8 | 1.22 | 341 | 0.09・0.18 | 0.29 | 0.3˜0.56 | −2 | | | | | 1000・1950 |
| RUN 003 | Test Run, Hovering Performance | 39 | 08.11/06 | 0 | 15.4 | 1.22 | 340 | 0 | 0 | 0.19˜0.56 | 0 | | 4～18 | 0 | 0 | 600～1800 |
| RUN 004 | Hovering Performance & Control Response | 39 | 08.11/06 | 0 | 15.4 | 1.22 | 340 | 0 | 0 | 0˜0.3 | 0 | | 6～18 | −2～2 | −2～2 | 1000 |
| RUN 005 | Forward Flight Conditions | 11 | 08.11/06 | 5～30 | 17 | 1.21 | 341 | 0˜0.09 | 0.05～0.29 | 0.31 | −2 | 3 | | | | 1000 |
| RUN 006 | Forward Flight Conditions | 11 | 08.11/06 | 5～30 | 17 | 1.21 | 341 | 0˜0.09 | 0.05～0.29 | 0.31 | −2 | 5 | | | | 1000 |
| RUN 007 | Forward Flight Conditions | 11 | 08.11/06 | 5～30 | 17 | 1.21 | 341 | 0˜0.09 | 0.05～0.29 | 0.31 | −2 | 6.4 | | | | 1000 |
| RUN 008 | Forward Flight Conditions & Control Response | 16 | 08.11/06 | 15 | 17 | 1.21 | 341 | 0˜0.09 | 0.14 | 0.31 | −2 | 5 | | −2～2 | −2～2 | 1000 |
| RUN 009 | Hovering Performance & Control Response | 35 | 08.11/07 | 0 | 17.2 | 1.20 | 342 | 0 | 0 | 0˜0.56 | 0 | | 6～14 | −2～2 | −2～2 | 1800 |
| RUN 010 | Forward Flight Conditions | 16 | 08.11/07 | 5～55 | 17.2 | 1.20 | 342 | 0˜0.16 | 0.05～0.29 | 0.56 | −2 | 3 | | | | 1800 |
| RUN 011 | Forward Flight Conditions | 16 | 08.11/07 | 5～55 | 17.2 | 1.20 | 342 | 0˜0.16 | 0.05～0.29 | 0.56 | −2 | 5 | | | | 1800 |
| RUN 012 | Forward Flight Conditions & Control Response | 16 | 08.11/07 | 25 | 17.2 | 1.20 | 342 | 0˜0.16 | 0.13 | 0.56 | −2 | 3 | | | | 1800 |
| RUN 013 | BVI Condition | 14 | 08.11/07 | 12～20 | 17.2 | 1.20 | 342 | 0˜0.16 | 0.11～0.19 | 0.31 | 4 | 8 | | | | 1000 |
| RUN 014 | BVI Condition | 14 | 08.11/07 | 12～20 | 17.2 | 1.20 | 342 | 0˜0.16 | 0.11～0.19 | 0.31 | 4 | 6.4 | | | | 1000 |
| RUN 022 | Hub drag, Fuselage pressure Measurement | 8 | 08.11/12 | 10～30 | 14 | 1.23 | 339 | 0˜0.08 | 0.09～0.28 | 0.31 | 4 | | | | | 1000 |


Figure 1: Photograph of JMRTS in JAXA 6.5mx5.5m Low-Speed Wind Tunnel

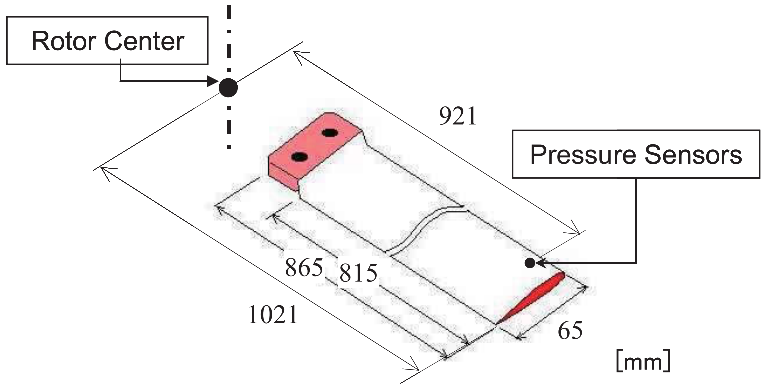


(a) Blade dimensions

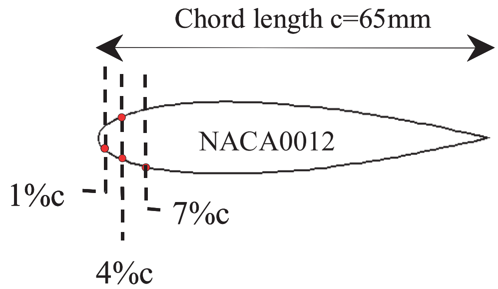


(b) Blade section with pressure sensors

Figure 2: Rotor blade

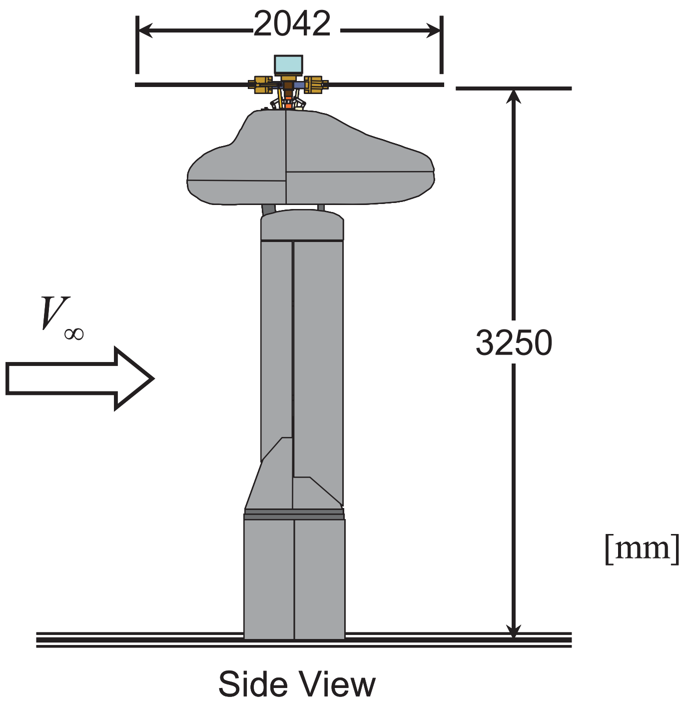


Figure 3: Side view of the rotor stand

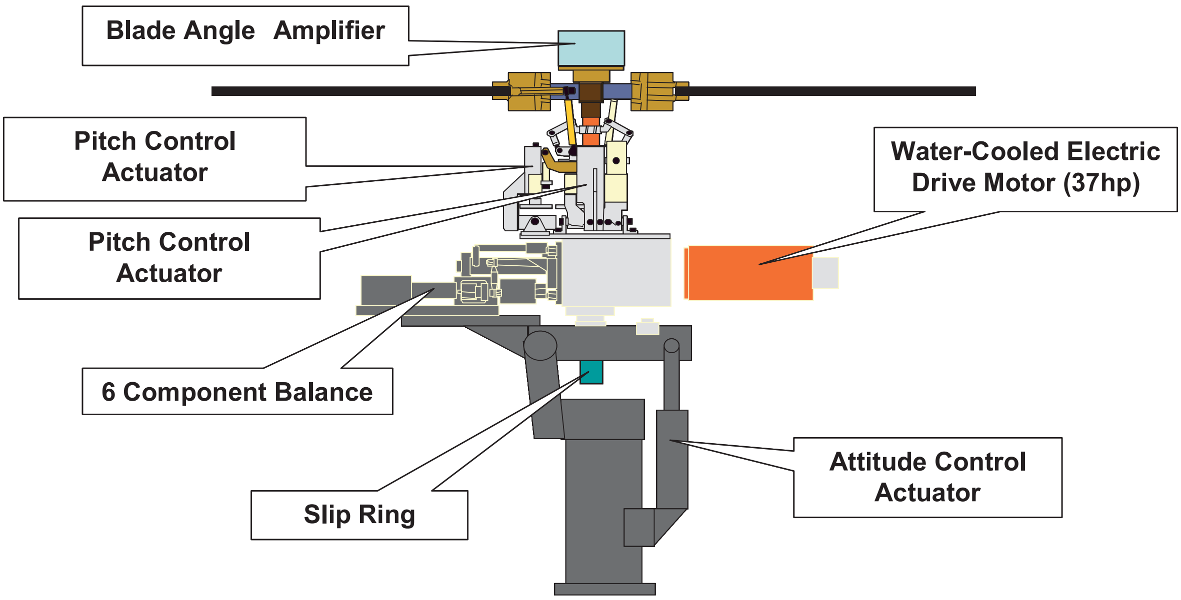


Figure 4: Main components of JMRTS

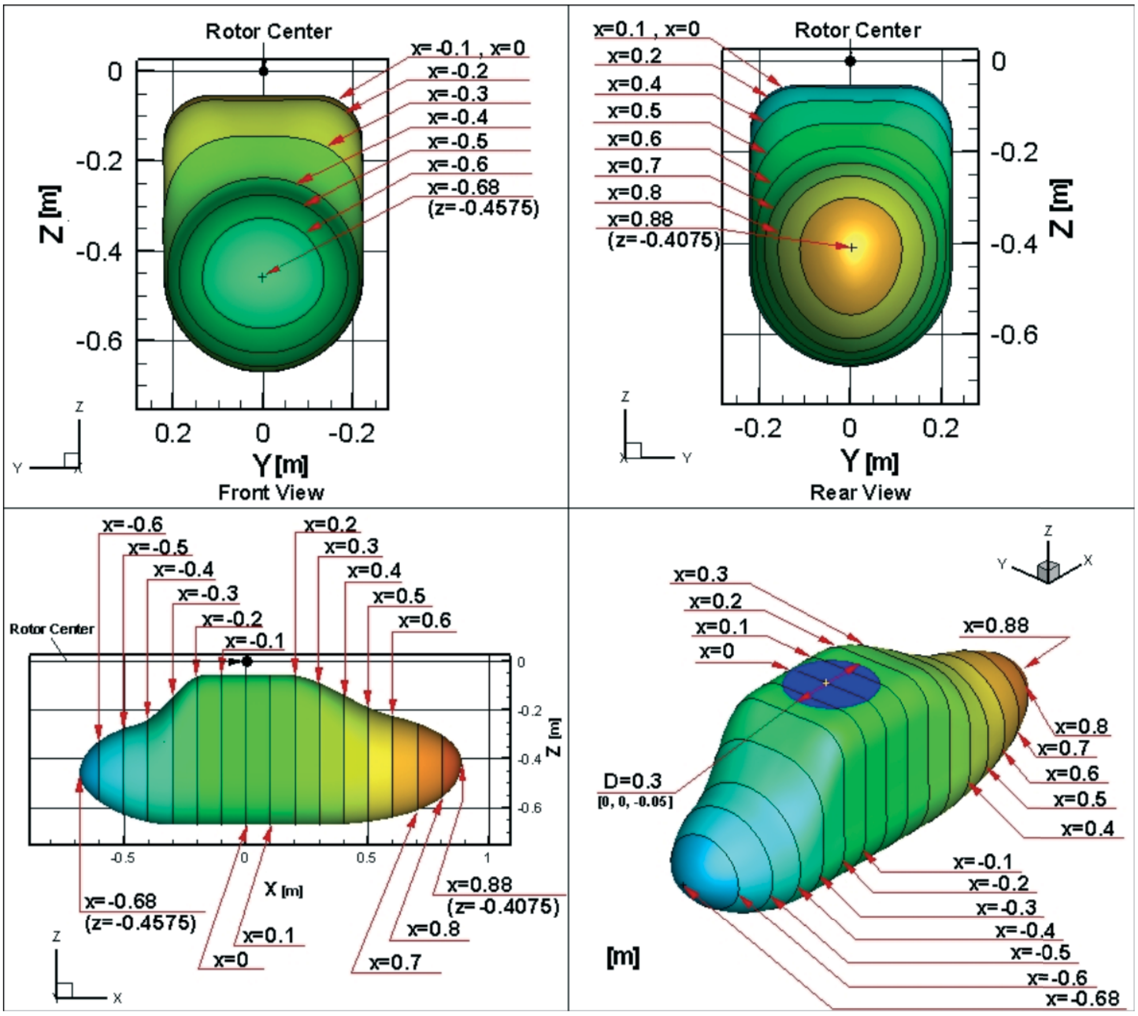


Figure 5 : Fuselage shape and contours (Axes origin at rotor center)

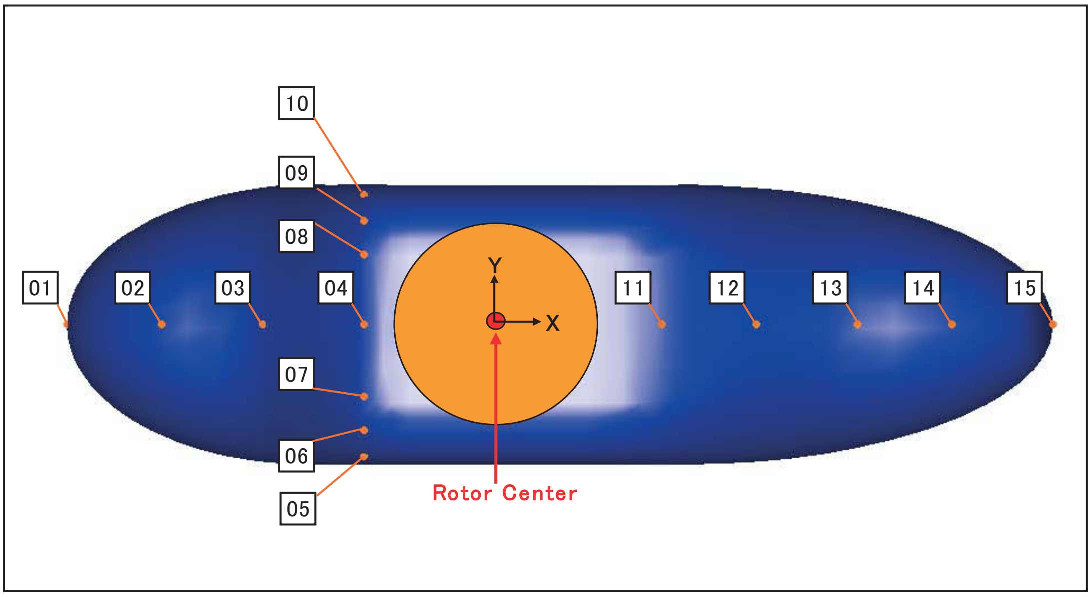


Figure 6 : Locations of unsteady pressure sensors on fuselage surface

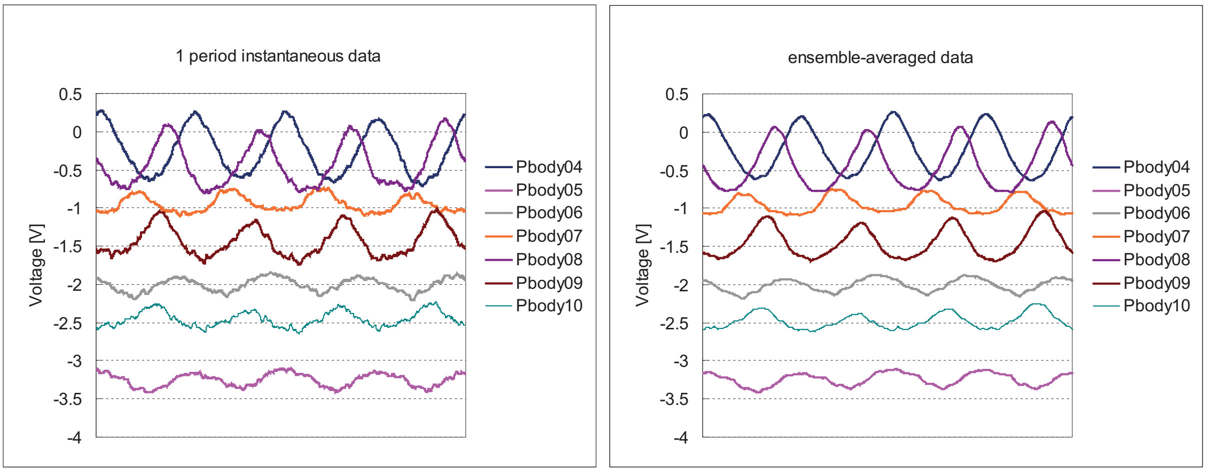


(a) Instantaneous (b) ensemble-averaged

Figure 7: Ensemble averaging of periodic data

Table 4: Detailed test conditions and averaged data for RUN011 (Mtip=0.56)

| Test condition | | | | | | | | | | | | |
|---|---|---|---|---|---|---|---|---|---|---|---|---|
| $\mu$ | 0 | 0.03 | 0.05 | 0.08 | 0.1 | 0.13 | 0.16 | 0.18 | 0.21 | 0.23 | 0.26 | 0.29 |
| $M_\infty$ | 0 | 0.015 | 0.029 | 0.044 | 0.059 | 0.073 | 0.088 | 0.102 | 0.117 | 0.131 | 0.146 | 0.161 |
| Mtip | 0.561 | 0.561 | 0.561 | 0.561 | 0.561 | 0.561 | 0.561 | 0.560 | 0.560 | 0.560 | 0.559 | 0.559 |
| $C_T \times 10^3$ | 2.97 | 4.78 | 4.77 | 4.79 | 4.76 | 4.80 | 4.80 | 4.78 | 4.81 | 4.77 | 4.76 | 4.78 |
| $\theta_0$ [deg] | 10.98 | 12.52 | 11.70 | 11.06 | 10.45 | 10.25 | 10.05 | 9.88 | 9.82 | 9.77 | 9.81 | 9.89 |
| A1 [deg] | −0.02 | −1.76 | −3.01 | −3.30 | −3.15 | −2.93 | −2.72 | −2.74 | −2.66 | −2.69 | −2.76 | −2.76 |
| B1 [deg] | 0.03 | 0.49 | 0.78 | 1.09 | 1.47 | 1.74 | 2.08 | 2.33 | 2.57 | 2.85 | 3.21 | 3.50 |
| $\alpha$ [deg] | −2 | −2 | −2 | −2 | −2 | −2 | −2 | −2 | −2 | −2 | −2 | −2 |

| averaged−6 component balance | | | | | | | | | | | | |
|---|---|---|---|---|---|---|---|---|---|---|---|---|
| $C_H$ | −1.07E−04 | −1.45E−04 | −1.00E−04 | −7.68E−05 | −4.59E−05 | −7.81E−06 | 4.24E−05 | 1.11E−04 | 1.97E−04 | 2.64E−04 | 3.39E−04 | 4.38E−04 |
| $C_Y$ | −3.38E−05 | −2.03E−04 | −2.71E−04 | −2.82E−04 | −2.67E−04 | −2.51E−04 | −2.44E−04 | −2.48E−04 | −2.72E−04 | −2.97E−04 | −2.92E−04 | −3.29E−04 |
| $C_T$ | 2.94E−03 | 4.74E−03 | 4.73E−03 | 4.75E−03 | 4.72E−03 | 4.76E−03 | 4.77E−03 | 4.75E−03 | 4.79E−03 | 4.76E−03 | 4.76E−03 | 4.78E−03 |
| $C_R$ | −1.65E−05 | 1.33E−06 | 1.04E−05 | 7.77E−06 | −1.53E−06 | −2.99E−06 | −1.52E−06 | −1.32E−06 | −3.62E−06 | −6.18E−06 | 4.16E−06 | −2.62E−06 |
| $C_M$ | −8.24E−06 | 9.07E−06 | 9.22E−06 | −3.82E−06 | −9.22E−06 | 3.89E−06 | −3.54E−06 | 5.27E−06 | 2.96E−05 | 1.25E−05 | 7.27E−06 | 1.71E−05 |
| $C_Q$ | 2.35E−04 | 3.37E−04 | 3.07E−04 | 2.76E−04 | 2.44E−04 | 2.27E−04 | 2.18E−04 | 2.09E−04 | 2.03E−04 | 1.99E−04 | 2.02E−04 | 2.01E−04 |

| blade angle | | | | | | | | | | | | |
|---|---|---|---|---|---|---|---|---|---|---|---|---|
| $\beta_0$ | 0.98 | 1.21 | 0.93 | 0.98 | 1.01 | 1.15 | 1.10 | 0.98 | 0.90 | 0.86 | 0.74 | 0.71 |
| $\beta_1$ | −0.05 | 0.12 | 0.14 | 0.13 | 0.17 | 0.18 | 0.05 | 0.21 | 0.18 | 0.21 | 0.24 | 0.23 |
| $\beta 2$ | −0.03 | −0.04 | −0.03 | −0.02 | −0.17 | −0.14 | −0.14 | −0.08 | −0.07 | −0.05 | −0.02 | 0.04 |
| $\theta_0$ | 10.98 | 12.52 | 11.70 | 11.06 | 10.45 | 10.25 | 10.05 | 9.88 | 9.82 | 9.77 | 9.81 | 9.89 |
| $\theta_1$ | 0.02 | 1.76 | 3.01 | 3.30 | 3.15 | 2.93 | 2.72 | 2.74 | 2.66 | 2.69 | 2.76 | 2.76 |
| $\theta 2$ | −0.03 | −0.49 | −0.78 | −1.09 | −1.47 | −1.74 | −2.08 | −2.33 | −2.57 | −2.85 | −3.21 | −3.50 |
| $\zeta_0$ | −1.01 | −1.24 | −1.47 | −1.33 | −1.22 | −1.03 | −1.06 | −1.18 | −1.26 | −1.31 | −1.45 | −1.53 |
| $\zeta_1$ | −0.06 | 0.15 | 0.19 | 0.16 | 0.20 | 0.20 | 0.05 | 0.22 | 0.20 | 0.21 | 0.24 | 0.20 |
| $\zeta 2$ | −0.04 | −0.07 | −0.06 | −0.06 | −0.23 | −0.18 | −0.17 | −0.10 | −0.07 | −0.06 | −0.02 | 0.06 |

| averaged−Cpa $\times 10^2$ | | | | | | | | | | | | |
|---|---|---|---|---|---|---|---|---|---|---|---|---|
| Pbody 01 | −0.228 | −0.134 | 0.063 | 0.171 | 0.319 | 0.506 | 0.737 | 1.002 | 1.318 | 1.671 | 2.067 | 2.503 |
| Pbody 02 | 0.133 | 0.205 | 0.050 | 0.101 | 0.143 | 0.191 | 0.244 | 0.302 | 0.368 | 0.435 | 0.511 | 0.600 |
| Pbody 03 | 0.117 | 0.201 | 0.181 | 0.135 | 0.236 | 0.362 | 0.513 | 0.685 | 0.889 | 1.112 | 1.366 | 1.648 |
| Pbody 04 | 0.052 | 0.159 | 0.181 | 0.138 | 0.120 | 0.135 | 0.109 | 0.070 | 0.003 | −0.080 | −0.182 | −0.300 |
| Pbody 05 | −0.090 | −0.307 | −0.352 | −0.236 | −0.478 | −0.751 | −1.098 | −1.504 | −1.989 | −2.515 | −3.102 | −3.756 |
| Pbody 06 | −0.026 | −0.096 | −0.139 | −0.198 | −0.303 | −0.469 | −0.693 | −0.960 | −1.293 | −1.658 | −2.057 | −2.494 |
| Pbody 07 | 0.066 | 0.085 | 0.087 | 0.014 | −0.036 | −0.098 | −0.204 | −0.336 | −0.514 | −0.717 | −0.946 | −1.186 |
| Pbody 08 | 0.047 | 0.181 | 0.200 | 0.161 | 0.118 | 0.094 | 0.039 | −0.030 | −0.132 | −0.256 | −0.384 | −0.536 |
| Pbody 09 | 0.054 | 0.136 | 0.108 | 0.044 | −0.066 | −0.185 | −0.361 | −0.569 | −0.824 | −1.113 | −1.433 | −1.791 |
| Pbody 10 | 0.031 | −0.023 | −0.103 | −0.162 | −0.284 | −0.505 | −0.786 | −1.124 | −1.535 | −1.988 | −2.490 | −3.048 |
| Pbody 11 | 0.138 | 0.151 | −0.098 | −0.124 | −0.179 | −0.246 | −0.319 | −0.412 | −0.540 | −0.653 | −0.795 | −0.985 |
| Pbody 12 | 0.167 | 0.185 | 0.060 | 0.007 | −0.063 | −0.141 | −0.220 | −0.318 | −0.436 | −0.591 | −0.775 | −0.939 |
| Pbody 13 | 0.176 | 0.254 | 0.118 | 0.035 | −0.012 | −0.074 | −0.129 | −0.205 | −0.275 | −0.384 | −0.467 | −0.593 |
| Pbody 14 | 0.139 | 0.189 | 0.045 | −0.012 | 0.010 | −0.019 | −0.035 | −0.067 | −0.095 | −0.136 | −0.141 | −0.204 |
| Pbody 15 | −0.196 | −0.418 | −0.059 | −0.010 | 0.011 | 0.018 | −0.001 | −0.027 | −0.055 | −0.104 | −0.139 | −0.197 |

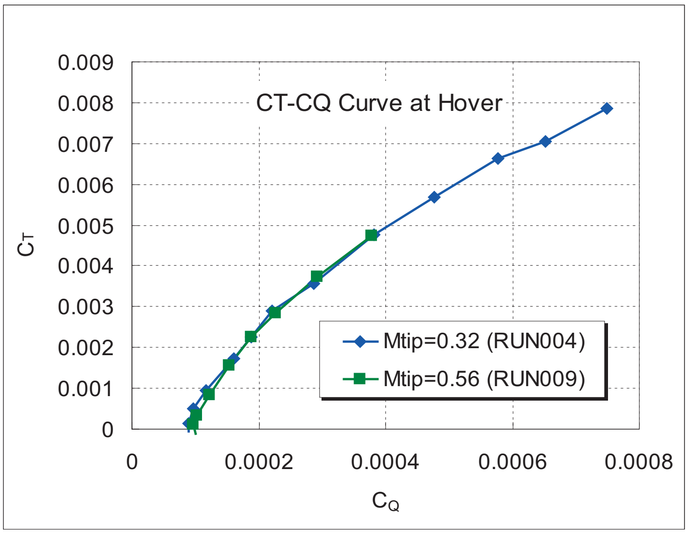


Figure 8 : CT-CQ curve at hover

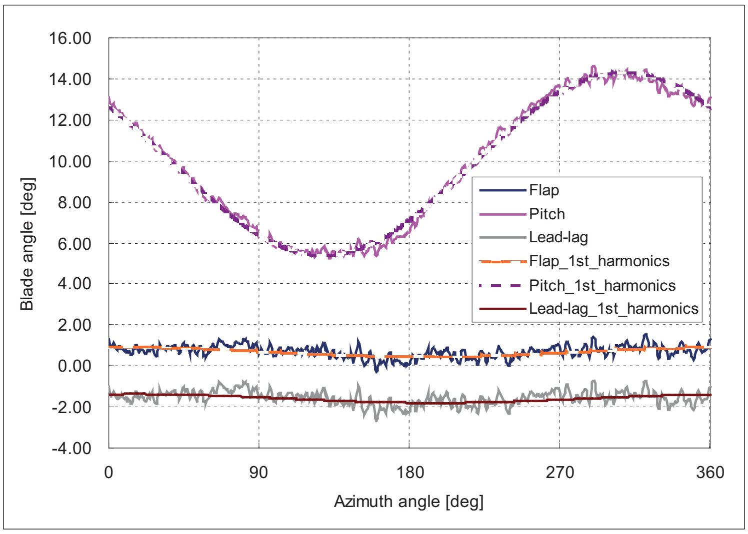


Figure 9 : Signals of blade angle sensors

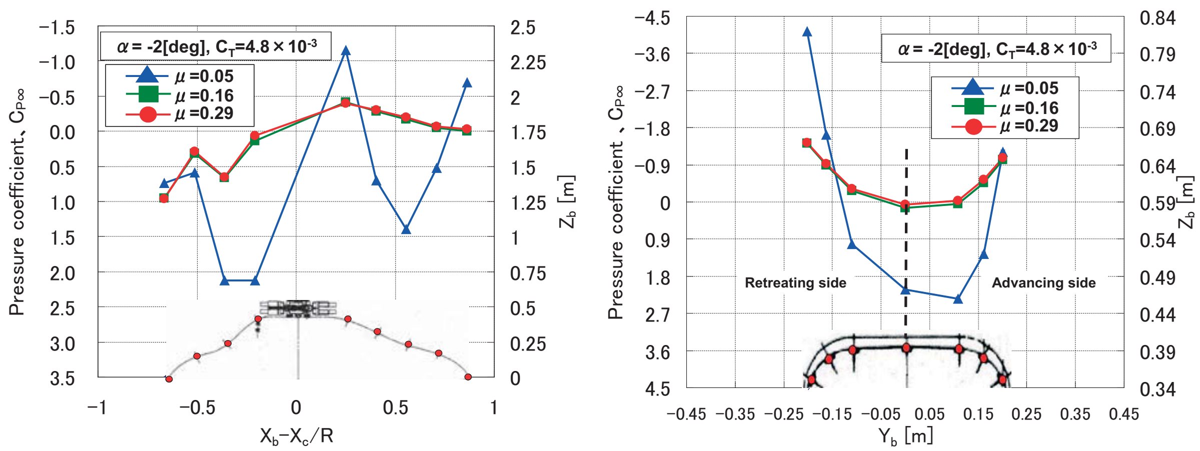


(a) Longitudinal line (b) Lateral line

Figure10 : Averaged surface pressure distribution with different advance ratios at Mtip=0.56

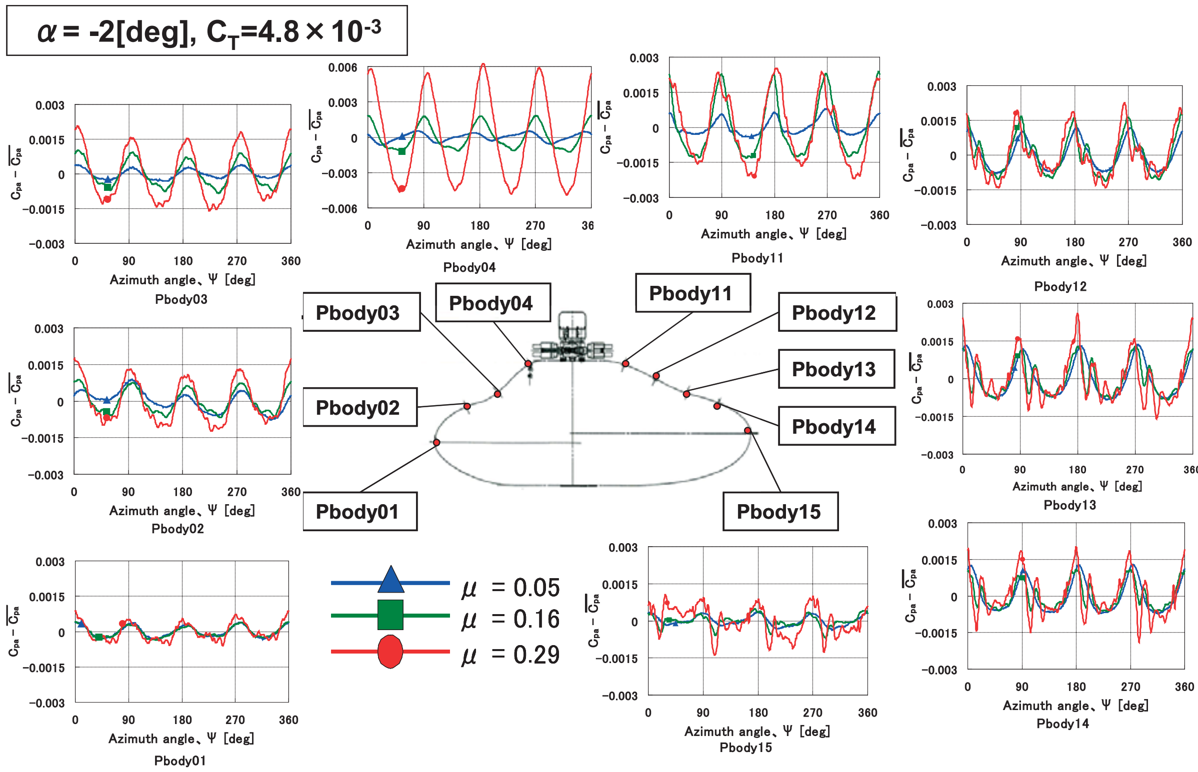


(a) Longitudinal line

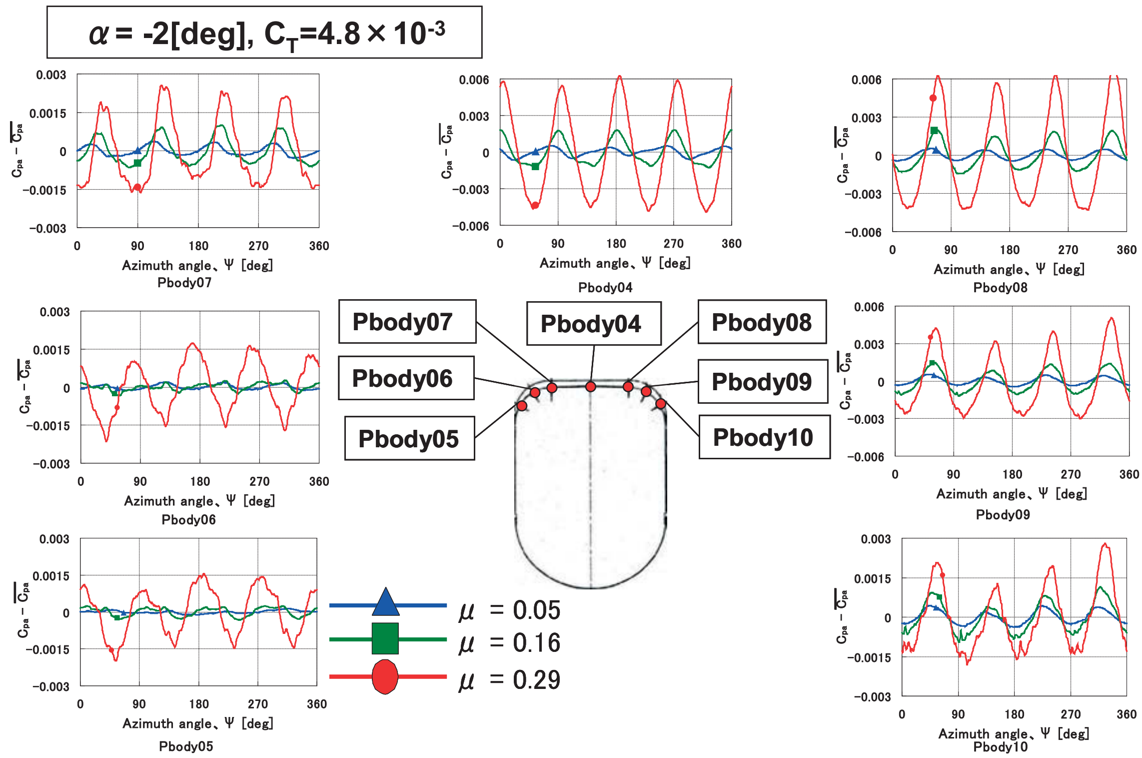


(b) Lateral line

Figure 11: Periodic variations of surface pressure with different advance ratios at Mtip=0.56